Experimental Investigation of a Small Drone Propeller Aerodynamics in Forward Flight

Experimental investigation of a small drone propeller aerodynamics in forward flight *

Grava Alessandro [†] [‡], Serpieri Jacopo [§], Iuso Gaetano [¶]
Polytechnic University of Turin, Corso Duca degli Abruzzi 24, 10129, Turin, Italy

Bernardos Luis[‖]
DAAA, ONERA, Polytechnic Institute of Paris, 92190, Meudon, France

Cafiero Gioacchino [**]
Polytechnic University of Turin, Corso Duca degli Abruzzi 24, 10129, Turin, Italy

The aerodynamic performance of small drones is difficult to be predicted. Their small-scale propellers operate in a challenging fluid dynamics regime characterized by low Reynolds numbers, where complex transitional phenomena usually occur around the blades' surface. In the present work, an experimental campaign is carried out on a small isolated propeller in forward flight conditions. The main scope is to investigate how the performance and the induced flow field are affected by the presence of a cross-flow, which can be representative of the forward flight condition for a typical drone's propeller. As the cross-flow velocity is incremented, considerable increases in thrust and power are measured. The resulting experimental loads are compared with semi-empirical laws derived from the momentum and blade element momentum theories. These laws have found an extensive use in the preliminary design of helicopters and are also found applicable to the hereby investigated propeller with appropriate tunings. Furthermore, an analysis of the propeller's wake is conducted via planar particle image velocimetry. Significant differences in terms of flow topology and flow field statistics are deducted with respect to the hovering condition. Ultimately, the vortices shed from the propeller's blades are identified and characterized and a focus is posed on the vortices' trajectory and circulation. With respect to the hovering condition, the strongest vortical structures are advected in more confined trajectories, while the weakest structures are instead broken down under the effect of the cross-flow.

*Presented as Paper AIAA 2024-0244 at the AIAA SciTech Forum 2024, 8-12 January 2024, Orlando, FL.
[†]Ph.D. Candidate, Department of Mechanical and Aerospace Engineering, AIAA Member
[‡]Corresponding Author, e-mail address: alessandro.grava@polito.it
[§]Assistant Professor, Department of Mechanical and Aerospace Engineering
[¶]Full Professor, Department of Mechanical and Aerospace Engineering
[‖]Aerodynamics Research Engineer, Aerodynamics, Aeroelasticity and Acoustic Department
[**]Associate Professor, Department of Mechanical and Aerospace Engineering, AIAA Member.

Nomenclature

A	=	propeller disk area [m^2], $A = \pi R^2$
c	=	blade chord [m]
c_m	=	blade mean chord [m]
c_{D_0}	=	blade profile drag coefficient at $\alpha = 0°$
c_{D_M}	=	mean blade profile drag coefficient
C_T	=	non-dimensional thrust coefficient, $C_T = \frac{T}{(\rho A(\Omega R)^2)}$
C_P	=	non-dimensional power coefficient, $C_P = \frac{P}{(\rho A(\Omega R)^3)}$
k	=	turbulent kinetic energy [m^2/s^2]
$k_{1,2,3}$	=	corrective coefficients for C_P interpolation
M	=	Mach number
n	=	revolutions per minute [rpm]
N_b	=	number of blades
N_{cr}	=	critical boundary layer disturbances integral amplification
P	=	consumed power [W]
Q	=	torque [Nm]
r	=	reference coordinate along the propeller radius [m]
R	=	propeller radius, $R = 7.5$ cm
Re_c	=	chord-based Reynolds number, $Re_c = \frac{cV_c}{\nu}$
T	=	thrust [N]
v_i	=	axial induced velocity [m/s]
V_x	=	velocity field component in the x axis [m/s]
V_y	=	velocity field component in the y axis [m/s]
$\overline{V_x}$,$\overline{V_y}$	=	time-averaged velocity components [m/s]
V'_x,V'_y	=	velocity fluctuations [m/s]
$\lvert\overline{V}\rvert$	=	absolute velocity magnitude [m/s], $\lvert\overline{V}\rvert = \sqrt{\overline{V_x}^2 + \overline{V_y}^2}$
V_∞	=	cross-flow velocity due to the forward flight motion [m/s]
V_c	=	inflow velocity in the chord-wise direction [m/s]
x	=	reference axis parallel to V_∞ [m]
y	=	reference axis perpendicular to V_∞ [m]
α	=	aerodynamic angle of attack [°]
α_{disk}	=	actuator disk's angle of attack [°]

Γ_v = tip-vortex circulation [m^2/s]

Γ_{2-thr} = arbitrary threshold value for the vortices centers identification

β = blade pitch angle [°]

λ_i = non-dimensional axial induced velocity, $\lambda_i = \frac{v_i}{\Omega R}$

μ = non-dimensional forward flight advance ratio, $\mu = \frac{V_\infty}{\Omega R}$

ν = air kinematic viscosity [m^2/s]

ρ = air density [kg/m^3]

σ = propeller solidity, $\sigma = \frac{N_b c_m}{\pi R}$

Φ = velocity vectors orientation with respect to V_∞ [°]

Ω = propeller angular speed [rad/s]

I. Introduction

The use of small drones, or Small Unmanned Aerial Vehicles (SUAVs), has surged in recent years, driven by advancements in technology in a wide range of applications. Significant investments are projected in the urban air mobility market, which is expected to grow steadily in the next years [1]. Potential application fields including the agriculture (e.g. [2]), aerial photography (e.g. [3]), and territorial monitoring (e.g. [4]) are beginning to rely upon the use of these small vehicles. However, as their popularity grows, so does the need for a deeper understanding of their aerodynamic performance to safely operate them in populated areas.

One of the most critical aspects concerns the aerodynamics of the propulsion system of these vehicles, which usually consists of multiple fixed-pitch propellers of reduced dimensions. These small-scale propellers typically exhibit chord-based Reynolds numbers (Re_c) lower than $5 \cdot 10^5$ along almost the entire span of the blade, thus belonging to the low Reynolds number regime [5]. In this regime, peculiar transitional phenomena occur on the blades' suction side, eventually affecting the overall performance of the propeller.

Lately, a large body of research has focused on the emerging field of small propellers aerodynamics with a particular focus on the hovering and axial inflow condition, representative of the take-off and the landing phase (e.g. [6–13]), and non-axial flow conditions (e.g. [14–20]), representative instead of the forward flight and the steady cruise conditions. The forward flight condition has been most of all extensively investigated in the past in the field of larger helicopters (e.g. [21–27]). Various analytical and semi-empirical relations have been derived in the literature, mostly based on the one dimensional momentum theory (1D MT) and the blade element momentum theory (BEMT) [21], to assess the performance variations as the flight speed is increased. However, it is not straightforward to transfer such approximations to the field of small UAVs, even though widely validated and still used in the preliminary design of large rotorcrafts. One reason is related to the different nature of the propulsive system, with variable pitch for helicopters and fixed pitch

for drones. A further reason is the different fluid dynamic regime that pertains to the two categories, mainly due to significant size and speed differences. Typical Re_c of helicopters rotor's blades results to be often greater than 10^6 [28], leading to a fully turbulent flow development around the blades.

Drones' propellers must be slightly tilted in the desired motion direction in order to operate in forward flight. Such tilt angle is influenced by several key parameters, including airspeed, weight, powertrain, and environmental conditions. Additionally, the design features of the drone, such as its propellers' size and configuration, play a significant role in determining the optimal tilt angle. As a general rule in performing a steady cruise flight, it is more efficient not to tilt excessively the propellers in the advance direction, maintaining a tilt angle very close to zero. This is typical in low speed flight operations in the field for agricultural spraying [2]. In these conditions, drone propellers operate at inflow angles close to 90° with respect to their rotation axis. Such inflow condition is hereby denominated cross-flow condition to address the relative wind orientation with respect to the propeller rotation axis. In the present work, the performance and the flow topology of a small two-bladed propeller are evaluated as the forward flight advance ratio μ is increased.

The scope of this paper is to experimentally investigate how a small two-bladed propeller is affected by the presence of a cross-flow, which can also be representative of a typical drone propeller in forward flight. In addition, the authors propose some modifications to the semi-empirical laws used for the helicopters' rotors, in order to transfer them to the performance prediction of small-scale fixed pitch propellers. Such laws might result in a useful tool to quickly assess the performance of a drone propeller under different flight conditions. Furthermore, the forward flight condition at such low Reynolds numbers proves challenging to be accurately predicted using computational methods, necessitating expensive high-fidelity numerical simulations. Thus this work aims to become a useful approach for future numerical analyses, being the propeller's geometry open and easily replicable. The shown results, in terms of performance and flow fields, might be furthermore considered to validate low fidelity computational tools. In conclusion, the authors aim to contribute to this emerging field with experimental data and semi-empirical tools which can be helpful in the improvement of small-scale propellers' design and performance prediction.

The remainder of the paper is organized as follows: in section II, the paper's methodology is presented. This includes a detailed description of the experimental setup, a subsection dedicated to the application of 1D MT and BEMT on helicopters' rotors in forward flight, and finally, a discussion on the methodology used for the vortex identification in the PIV fields. The measured thrust and torque changes are shown and discussed in section III in terms of non-dimensional coefficients as a function of μ. The experimental data are consequently compared with the semi-empirical formula available in literature for helicopters preliminary design, in order to assess their transferability to small fixed-pitch propellers. In the same section, the flow field surrounding the propeller is thoroughly investigated with the use of the planar particle image velocimetry (PIV) and the results in terms of first and second order statistics are shown. A focus on the vortical structures generated by the propeller's blades is consequently made. Finally, in section IV, a conclusive summary is given.

II. Methodology

A. Experimental Setup

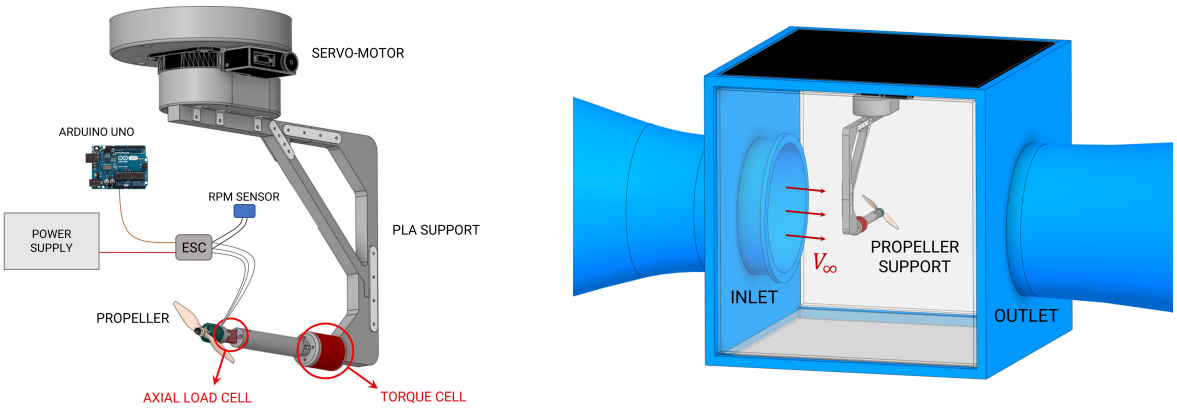

Fig. 1 Schematic representation of the experimental setup.

The experiments were performed in the "Ferrari" open circuit wind tunnel at Politecnico di Torino, with the experimental setup illustrated in figure 1. The wind tunnel presents a honeycomb and two mesh screens at its inlet section, followed by a contraction with area ratio of 3.25:1, leading into a cubic enclosed open test section having a side equal to 88 cm. The propeller support was mounted at a streamwise distance from the inlet of the test section equal to 44 cm. A preliminary characterization of the flow has revealed that the mean flow profile is uniform across a span of about 30 cm, with a turbulence intensity level below 1%.

Focusing on the propeller and its support, the main components are presented in figure 1 and herein briefly described. The propeller was 3D printed in VisiJet Armor M2G-CL resin. The model's geometry was defined by taking the propeller employed in [29] as a reference and then scaling it for the current purpose to a propeller with a radius $R = 7.5$ cm. It derives from a two-bladed APC-96 model, by reshaping each profile from $r/R = 0.2$ to the tip with a NACA 4412 profile, being r the radial reference coordinate along R. An elliptical root section is merged with such profiles starting from the hub to the station $r/R = 0.2$. In figure 2, the exact non-dimensional chord (c/R) and pitch angle (β) distributions are reported as a function of r/R.

The choice of this model presents multiple advantages with respect to an off-the-shelf design, including the possibility to compare the results with those available in the literature, at least from the thrust and consumed power point of view. Moreover, this allows for the exact knowledge of the geometry for ongoing and future numerical analyses.

The drivetrain is constituted by a TRX370 1000KV brushless motor with a diameter of 2.8 cm and a maximum power of 150 W. The motor is controlled by an external electronic speed controller (ESC) which receives the input commands through an Arduino Uno board. The rotational speed of the shaft is measured using an Hobbywing RPM sensor which is connected to two of three phases of the brushless motor. The sensor counts the voltage changes at the

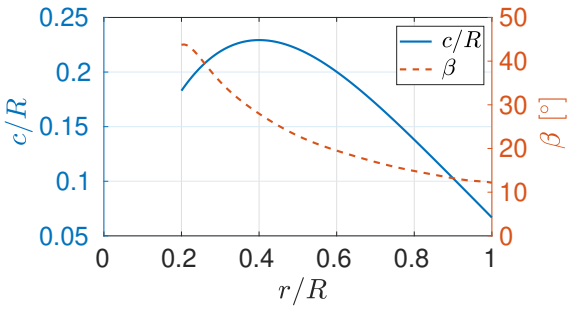

Fig. 2 Propeller's blades chord and pitch angle distribution as a function of r/R, re-scaled starting from [29]

two phases within a time interval of 0.1 s and converts the information to a value of n. The sensor has a rated output which ranges from n = 1000 rpm to n = 300000 rpm for the case of a 2 poles motor, as the one hereby considered. The absolute error in maintaining a fixed n = 3000 was estimated to be around ± 10 rpm with the considered drivetrain.

The drivetrain was mounted on a 3D printed support realized in polyactic acid (PLA). The support shape was designed to host two load sensors in order to evaluate the propeller thrust and consumed power. To this end, a bi-directional axial load cell LSB201 Futek excited with 5 V was chosen for the thrust measurements. It is characterized by a rated output (RO) of 2.5 N, non-linearity and hysteresis of ± 0.1% of RO and an operating temperature range of 223–365 K.

A TFF400 Futek torque sensor excited with 10 V was instead considered for the torque measurements. Thanks to the acquisition of the motor's rotational speed Ω, it is straightforward to obtain the power consumption from the torque measurements as $P = Q\Omega$. The torque sensor is characterized by a RO of 0.07 Nm, non-linearity and hysteresis of ± 0.2% of RO and an operating temperature range of 223–365 K. The sensor is mounted at a distance of about three times the radius R downstream the propeller, in order to limit its blockage effects [30–33]. The propeller's thrust and torque are acquired over a sampling time of 120 seconds at a sampling frequency of 10 kHz.

The PLA support is connected to a Optosigma OSMS-120YAW servo-motor, which allows a 360° rotation around the vertical axis passing through the propeller's hub.

The flow field surrounding the propeller was investigated through planar PIV in two different regions of interest (ROI), illustrated in figures 3.(a) (fore ROI) and 3.(b) (aft ROI). The two regions are located at the centerline plane, respectively upstream and downstream of the propeller support.

The reference system reported in figures 3.(a) and 3.(b) was chosen in order to describe the investigated plane in the two ROI. Its origin is placed in correspondence of the propeller's hub and the two coordinates x and y are normalized with respect to the propeller's radius R. The cross-flow velocity (V_∞) direction aligns with the x axis, whereas the propeller rotation axis is oriented in the y axis direction. A Dantec Dynamics Nd:YAG Dual Power 200 laser (200 mJ/pulse, 15 Hz maximum repetition rate) operated in dual pulse mode was used to illuminate the tracing particles. The

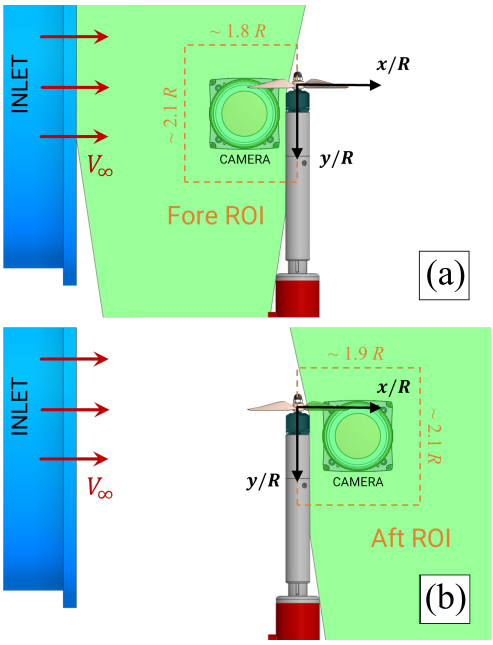

Fig. 3 Top view of the investigated regions in the planar PIV measurements. (a) fore ROI, (b) aft ROI.

laser was shaped into a thin sheet using an optical setup consisting of a set of opportune lens and illuminated the fore and the aft ROI.

One Andor Zyla 5.5 Mpx sCMOS camera (sensor size of 2560x2160 pixel^2, pixel size of 6.5 μm, 16 bits) was used to capture images of the illuminated tracing particles. The camera was synchronized with the laser system using a NI - PCIe 6612. The camera was equipped with a Nikon 60 mm Macro lens, with a value of the aperture $f_\# = 8$. The optical resolution resulted to be approximately 13.2 px. The investigation area extended for about 1.8 R x 2.1 R (13.5 x 15.7 cm^2) in the fore ROI, whereas for approximately 1.9 R x 2.1 R (14.2 x 15.7 cm^2) in the aft ROI. The tests' acquisition frequency was set to 14.1175 Hz, in order to avoid phase-locked measurements and ensure well-converged statistics. The phase-shift between two different images pairs results to be of 14.4° with n = 3000 rpm. This phase-shift is additionally affected by the drivetrain accuracy in maintaining a fixed value of n, ensuring a wider phases dataset.

The flow was seeded upstream of the contraction using a Laskin nozzle which produces particles of about 1 μm fueled with the high performance seeding fluid 'PIVLIGHT'.

Each measurement consisted of 2500 images pairs. The raw images were first pre-processed with an historical minimum subtraction to reduce the light reflection from the propeller blades and the support. The vector fields were obtained by processing the collected images using a correlation based algorithm. A spline interpolation of the images and the velocity fields was performed, as recommended by [34, 35]. A Blackmann weighting window was used to tune the spatial resolution [36]. The algorithm is based on a multi-pass approach and the final interrogation window size was 32 x 32 pixels^2 (2.4 x 2.4 mm^2), with 75% overlap, corresponding to a final vector spacing of about 8e-3R (0.6

mm). The PIV measurements were carried out imposing a time delay between the two frames which led to a mean displacement of the tracer particles of about 12 pixels. Considering the common figure of an absolute error of 0.1 pixels on the mean field, the error can be then estimated as lower than 0.1% on the averaged quantities. Conversely, the error on the second order statistics and the computation of the vorticity component is less than 5% [37]. The turbulent kinetic energy k and Reynolds stresses were furthermore post-processed with the use of a six-sigma to reduce the effect on any spurious vectors on such higher order statistics.

The load sensors measurements were conducted at a fixed value of n = 3000, while V_∞ ranged from 0 m/s to 15 m/s with a step of 1 m/s, thus corresponding to values of μ between 0 to 0.64. The PIV tests were exclusively conducted at inflow velocities between V_∞ = 0 m/s and V_∞ = 5 m/s. The blades' chord-based Reynolds number Re_c varies along the blade-span between 5000 and 15000, depending on the radial station r/R where it is is calculated and the local velocity due to the influence of the external cross-flow.

B. Theoretical background

The forward flight condition has been extensively studied for the helicopters' design and some successful approximations to predict their performance have been formulated over the years [21]. The scope of the present subsection is to briefly summarize the main points and results of these studies. Among the simplest theories, the one dimensional momentum theory (1D MT) was initially modified to be applicable in the context of propellers and rotors in forward flight [38]. In this condition, the inflow velocity vector V_∞ presents a significantly high angle of attack α_{disk} with respect to the actuator disk's rotation axis, as illustrated in figure 4.

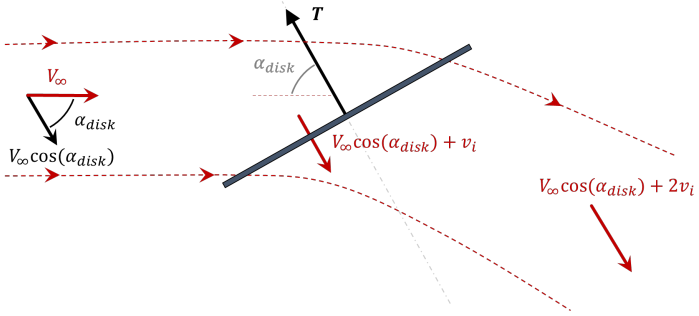

Fig. 4 Actuator disk model in forward flight conditions.

From the momentum and energy balance, it is possible to derive eq. 1 for the thrust T, which depends on the induced velocity on the actuator disk v_i, α_{disk} and the forward flight velocity V_∞, given a fixed geometry.

$$T = 2\rho A v_i \sqrt{v_i^2 + 2V_\infty v_i cos(\alpha_{disk}) + V_\infty^2} \tag{1}$$

According to this approach, the induced velocity is assumed to be constant over the entire surface of the actuator

disk. In eq. 1, the term $cos(\alpha_{disk})$ can be neglected when the angle is close to 90°. The simplified eq. 1 can be also reported in non-dimensional terms, as in eq. 2, being λ_i the non-dimensional induced velocity.

$$C_T = 2\lambda_i\sqrt{\lambda_i^2 + \mu^2} \tag{2}$$

Eq. 2 is representative of the operative conditions analysed in the present work and more generally of a propeller in cross-flow. From eq. 2 it is possible to isolate the induced velocity λ_i as a function of C_T and μ. The absence of the cosine term provide indeed for a simple analytical solution, reported in eq. 3.

$$\lambda_i = \sqrt{-\frac{\mu^2}{2} \pm \frac{\sqrt{\mu^4 + C_T^2}}{2}} \tag{3}$$

At considerably high μ, the quantity λ_i results to be negligible with respect to μ, leading to the so-called Glauert high speed approximation (GHS) [38], reported in eq. 4.

$$C_T = 2\mu\lambda_{i-GHS} \tag{4}$$

Even in this simplified case it is possible to isolate the non-dimensional induced velocity λ_{i-GHS} as in eq. 5.

$$\lambda_{i-GHS} = \frac{C_T}{2\mu} \tag{5}$$

The consumed power of a rotary wing aircraft can be instead evaluated as the sum of three contributions: the non-dimensional induced power C_{P_i}, the profile power C_{P_0} and the parasitic power C_{P_p} [39].

The induced power is the power required to produce the thrust. With the use of the 1D MT, the non-dimensional induced power coefficient can be written as in eq. 6, being k_1 an empirical corrective coefficient typically around 1.15 for the helicopters' rotors [39] (R2).

$$C_{P_i} = k_1 C_T \lambda_i \tag{6}$$

The profile power is the power required to overcome the blades profile drag. With the use of BEMT, it can be evaluated with eq. 7, being σ is the blades solidity, c_{D_M} is the mean blade profile drag coefficient and k_2 a further corrective coefficient, which is usually taken between 4.5-4.7 in the helicopters' preliminary design [40].

$$C_{P_0} = \frac{\sigma c_{D_M}}{8}(1 + k_2\mu^2) \tag{7}$$

The calculation of c_{D_M} requires a knowledge of the blades' airfoil geometry and the Reynolds number, Mach

number and angle of attack. For what concerns helicopters' rotors, their blades' are usually characterized by a constant or very small pitch angle along the blade radius. In addition, they are operated at low angles of attack and higher Reynolds numbers for an improved aerodynamic efficiency. Given these premises, the typical $c_D - \alpha$ curves thus result to be nearly constant at contained angles of attack. As a first approximation, it is thus possible to consider $c_{D_M} \sim c_{D_0}$, with c_{D_0} being the blade profile drag coefficient at zero angle of attack. For what regards instead the small propeller taken into account in this work, it is designed with a considerably high and variable pitch angle along the blade-span 2 and a chord-based Reynolds number which varies approximately between 5000 and 15000. In this range, the polar curves present a less immediate behaviour which is still under investigation [41, 42]. To obtain a first approximation of the NACA 4412 polars at these very low Reynolds numbers, the software XFoil [43] is exploited. The $c_D - \alpha$ curves obtained with XFoil at Re_c = 5000, 10000 and 15000 and a Mach number M = 0.1 are reported in figure 5. The curves are obtained by considering the boundary layer disturbances integral amplification evaluated at the transition location (N_{cr}) equal to 9. This parameter is used as an indication of the free flow turbulence and is used to simulate the natural transition location, according to the e^N theory [44].

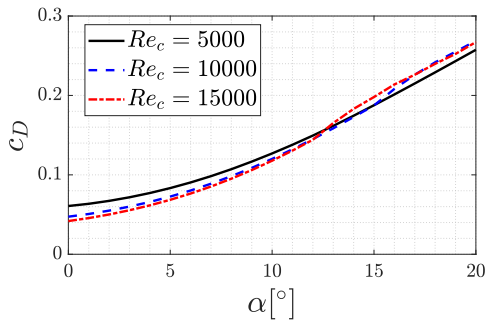

Fig. 5 Drag coefficient (c_D) as a function of the angle of attack (α) for the NACA 4412 airfoil at Re_c = 5000, 10000 and 15000 and M = 0.1. The curves are obtained with XFoil, imposing N_{cr} = 9.

The resulting value of c_{D_0} is 0.05 in the considered Re_c range. Differently from higher Reynolds numbers, c_D considerably increases with α even at contained angles of attack. Therefore, the approximation of $c_{D_M} \sim c_{D_0}$ results to be inaccurate for the considered propeller and it is necessary to take into account an additional corrective coefficient k_3. The mean drag coefficient can be hence written as: $c_{D_M} = k_3 c_{D_0}$, with k_3 to be empirically evaluated.

The last contribution C_{P_p} is due to the necessary power to overcome the drag of the aircraft and it is consequently neglected in this analysis.

The resulting semi-empirical formulation describing C_P as a function of μ is finally reported in equation 8.

$$C_P = k_1 C_T \lambda_i + \frac{\sigma k_3 c_{D_0}}{8}(1 + k_2 \mu^2) \tag{8}$$

In the present work, eq. 2 and 8 are taken into account to fit the experimental data. However, it is fundamental to

highlight the absence of a third relation linking λ_i to μ to close the problem. For this reason, eq. 2 is used to derive the λ_i trend as a function of μ, given the experimental non-dimensional thrust ($C_{T_{EXP}}$) as an input. $C_{T_{EXP}}$ and λ_i values are then used in the equation 8 to fit the semi-empirical equation with the corresponding experimental power results ($C_{P_{EXP}}$) measured with the torque sensor. The fitting is carried out with the least squared method, using k_1, k_2 and k_3 as free interpolation coefficients.

C. Vortex characterization

In order to quantify how the presence of the cross-flow affects the vortical structures in the propeller's wake, a vortex identification and characterization method is exploited. Multiple methods exist in the literature and have become rather popular in the past years [45]. In the classical fluid mechanics theories, vortices are thought as regions of high vorticity. The simplest detection method is indeed based on the relation between local vorticity maxima and vortex centers. However, this presents some intrinsic flaws, not being able to accurately predict the vortex center when a shear flow is superimposed to pure rotation [45]. In order to cope with this problem, different gradient based approaches have been proposed in the literature. These methods are Galilean invariant, due to the independence of the velocity gradient tensor from the considered inertial system. Furthermore, they are based on a threshold, which permits to distinguish among regions with a prevalence of rotation with respect to those regions where the strain instead dominates. Such threshold can either be physics-related or arbitrary. To cite some, one might mention the Q-criterion [46], the Δ-criterion [47] and the λ_2-criterion [45]. Despite of being the state-of-art of vortex identification criteria in multiple applications, they might not work properly if applied to PIV data, where experimental noise is also present. In [48], the authors tested the effectiveness of different methods for the identification of the tip-vortices shed by a small helicopter rotor. Inaccuracies in the velocity fields computation due to laser reflections on the blades, lack of seeding and low signal-to-noise ratio put a strain on the velocity gradient based methods resulting in a often inaccurate vortices identification. To overcome such limitations, a further method introduced in [49] and widely used in the PIV fields analysis [50–52] was taken into account by De Gregorio et al. for a comparison. The method, based on a scalar function Γ_2, relies only upon the local flow topology, avoiding the computation of the velocity gradient and so resulting to be more robust for PIV data. In particular, let P be a fixed point in the 2D rectangular grid where the velocity is evaluated through the PIV technique. It is possible to define a dimensionless scalar denominated Γ_2 in the point P as in eq. 9,being S a rectangular domain of fixed size which surrounds P, M a point in S, $\overline{PM}$ the vector which links the two points, and z a normal vector to the considered plane.

$$\Gamma_2(P) = \frac{1}{N} \sum_S \frac{[\overline{PM} \wedge (U_M - \overline{U_P})] \cdot z}{\|\overline{PM}\| \cdot \|U_M - \overline{U_P}\|} \tag{9}$$

In the limit of $S \to 0$, it can be shown that Γ_2 is only a function of the rotation rate corresponding to the

anti-symmetrical part of the velocity gradient and the eigenvalue of the tensor's symmetrical part [49]. Despite of the still unknown exact relation between $|\Gamma_2|$ and the two quantities, it is shown that it is possible to discriminate among regions dominated by strain ($|\Gamma_2| < 2/\pi$), regions of pure shear ($|\Gamma_2| = 2/\pi$) and regions of the flow dominated by rotation ($|\Gamma_2| > 2/\pi$) [49]. The overall method hence represents a robust way to identify vortical structures. On the other hand, the vortex dimensions evaluation is instead highly dependent on the chosen value for N. For this purpose, in [51] it is suggested to choose N in order to evaluate the two scalar functions in a domain S of the order of the tip-vortices present in the flow field. The vortices centers can be identified at this stage in correspondence of local $|\Gamma_2|$ maxima which overcome an arbitrary threshold Γ_{2-thr}. The vortex area is then evaluated around the center and it is retained to extend until $|\Gamma_2| > 2/\pi$ in the surrounding singularly connected region. Once the area is evaluated, making use of the Stokes-Kelvin theorem, it is possible to compute the vortex circulation as the integral of the vorticity. The choice of the parameter N instead significantly influences the calculation of both vortices area and circulation. In particular, the vortex area is subjected to a magnification with the increase of N. This inevitably leads to non-negligible uncertainties on the exact area and circulation values. Fixing the value for N, however, will allow a comparative assessment of the area of the vortices among the investigated cases.

III. Results

In the present section, the results in terms of the propeller's aerodynamic performance are initially shown and discussed. The time-averaged non-dimensional thrust and power coefficients are reported as a function of the forward flight advance ratio μ. The semi-empirical relations introduced in section II.B are hereby taken into consideration to fit the $C_{P_{EXP}}$ data with the least squares method. Afterwards, the main time-averaged flow field features obtained through the planar PIV are presented. In the analyzed fore and aft ROI, the velocity fields are presented in terms of $|\overline{V}|$ and $\overline{V_y}$. In a second instance, higher order statistics such as the turbulent kinetic energy k and Reynolds stresses cross component $\overline{V_x' V_y'}$ are shown and thoroughly discussed. Ultimately, the vortices identified with the use of the Γ_2 criterion are characterized in their main features. In particular, a focus is made on their trajectory and circulation. The results are presented in a non-dimensional form, using Ω and R as reference quantities.

A. Propeller's aerodynamic performance

The $C_{T_{EXP}}$ results are reported as a function of μ in figure 6. $C_{T_{EXP}}$ displays a monotically increasing trend as a function of μ in figure 6. At small μ values, the $C_{T_{EXP}}$ growth appears to be contained. As μ is increased above 0.1, the thrust shows a steeper increase, establishing a quasi-linear trend.

Eqs. 3 and 5 are now taken into account to evaluate the trend of λ_i and λ_{i-GHS}as a function of μ. To this aim, the $C_{T_{EXP}}$ values showed in figure 6 are used in the equations and the results are displayed in figure 7. The dimensionless induced velocity λ_i obtained from the equation 2 exhibits a monotonically decreasing trend, starting from the initial

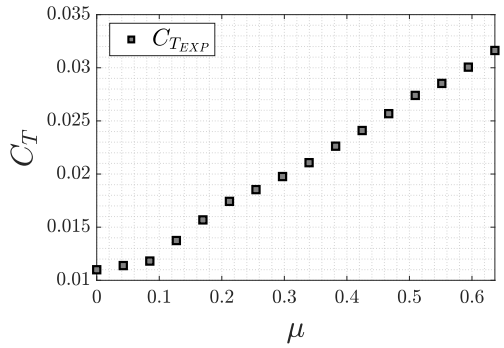

Fig. 6 Experimental time-averaged thrust coefficients $C_{T_{EXP}}$ as a function of μ.

value obtained for the hovering condition at $\mu = 0$. Such decrease appears steeper for small μ values, but becomes considerably smaller as μ increases. The induced velocity evaluated with the GHS approximation λ_{i-GHS} shows a similar trend, overlapping on the λ_i values from $\mu > 0.15$. For lower μ values, this approximation loses its validity, leading to λ_{i-GHS} values which tend to infinite as μ approaches the null value.

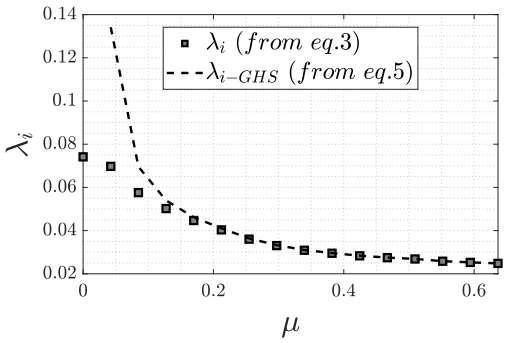

Fig. 7 Non-dimensional induced velocity λ_i as a function of μ, calculated with the equations 2 and 4 and imposing $C_T = C_{T_{EXP}}$.

In figure 8, the non-dimensional consumed power $C_{P_{EXP}}$ is displayed as a function of μ. The same plot also includes the interpolation of the experimental data obtained using the equation 8 with k_1, k_2, and k_3 as the free interpolation coefficients. A first interpolation is carried out on the totality of the experimental points ($C_{P_{FIT}}$). Furthermore, a second interpolation is carried out by only taking into account the points for $\mu > 0.15$ ($C_{P_{FIT-GHS}}$), hence pertaining to the range of μ where the GHS approximation was shown to be valid. The curves shown in the figure represent the best fittings obtained and the values assumed by the free interpolation coefficients are summarized in table 1.

The experimental consumed power $C_{P_{EXP}}$ presents a plateau at contained μ values, to then monotonically increase as μ is increased above around 0.1. The fitting curve $C_{P_{FIT}}$, represented with a solid red-colored line in figure 8, results to accurately approximate the $C_{P_{EXP}}$ data in the considered μ range. The $C_{P_{FIT}}$ curve deviates more significantly from the experimental data in the hovering condition ($\mu = 0$) and for μ values between 0.21 and 0.38. Even in these cases,

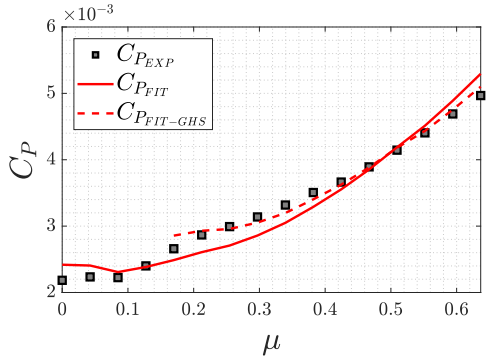

Fig. 8 Experimental time-averaged power coefficients $C_{P_{EXP}}$ as a function of μ compared with the best fitting curves obtained from the semi-empirical formula in eq. 8. The interpolation is respectively carried out on the entire experimental data set ($C_{P_{FIT}}$, continuous red line) and for $\mu > 0.15$ ($C_{P_{FIT-GHS}}$, dashed red line).

	k_1	k_2	k_3
Literature	1.15	4.5-4.7	-
$C_{P_{FIT}}$	1.20	5.00	1.82
$C_{P_{FIT-GHS}}$	2.05	4.67	1.53

Table 1 Corrective coefficients obtained from the $C_{P_{EXP}}$ data interpolation. The coefficients k_1 and k_2 used in literature [39, 40] for helicopters in forward flight are also reported for the sake of comparison.

the relative error among the data does not however exceed the 10 %. The corrective coefficients k_1 and k_2 of this first fitting result to be very close to the values used in the helicopters' preliminary design, as displayed in table 1. The third corrective coefficient k_3 can be multiplied by the blades' airfoil c_{D_0} in order to obtain an approximation of the profile mean drag coefficient c_{D_M} for the given propeller in forward flight conditions. In the same figure, the $C_{P_{FIT-GHS}}$ fitting curve is displayed with a dashed red-colored line. The curve is obtained and plotted for $\mu > 0.15$, according to the observations made for the results in figure 7 regarding the GHS approximation validity. The interpolation results to be even more accurate, with relative errors averagely contained under the 3 % and a maximum relative error equal to the 7 % at $\mu = 0.15$. In this case, k_2 is closer to the literature value with respect to the $C_{P_{FIT}}$ fitting, however k_1 instead considerably increased, as shown in table 1. In conclusion, k_3 is closer to 1, indication that c_{D_M} is closer to c_{D_0} in the GHS approximation.

The quality of the two interpolations can be additionally inferred from the evaluation of the coefficient of determination R^2 [53]. The coefficient quantifies the proportion of variance in the dependent variable ($C_{P_{FIT}}$ or $C_{P_{FIT-GHS}}$) that is predictable from the independent variable ($C_{P_{EXP}}$). The resulting R^2 values are respectively equal to 95 % for the $C_{P_{FIT}}$ fitting and 98 % for the $C_{P_{FIT-GHS}}$ fitting. Such results suggest an excellent data fitting and the choice of an adequate semi-empirical model for the scope. The fitting coefficients k_1 and k_2 result to be close to the literature values, mostly in the first interpolation on the larger μ range. Some differences were however expected due to the

propeller's low Reynolds number and the blades' high pitch, as thoroughly discussed in section II.B. Moreover, there was the necessity of introducing a third coefficient k_3 to approximate c_{D_M} directly from c_{D_0}. The value of k_3 is most likely non-generalizable to different geometries or operative conditions, however it should not be excluded that further experimental campaigns might lead to a value of k_3 which can be ultimately generalized in the field of small-scale propellers.

B. Time-averaged flow features

The most relevant flow topology features are assessed with the use of the planar PIV. In particular, the investigated operative conditions are representative of the hovering condition ($\mu = 0$) and contained forward flight velocity ($\mu = 0.04$, 0.08, 0.13, 0.17, 0.21). The operative conditions taken into account correspond to the first six data points of figures 6, 7 and 8. For what concerns the time-averaged velocity fields, the colormaps of the non-dimensional absolute velocity magnitude $|\overline{V}|/\Omega R$ fields with overlaid streamlines are reported in figure 9.

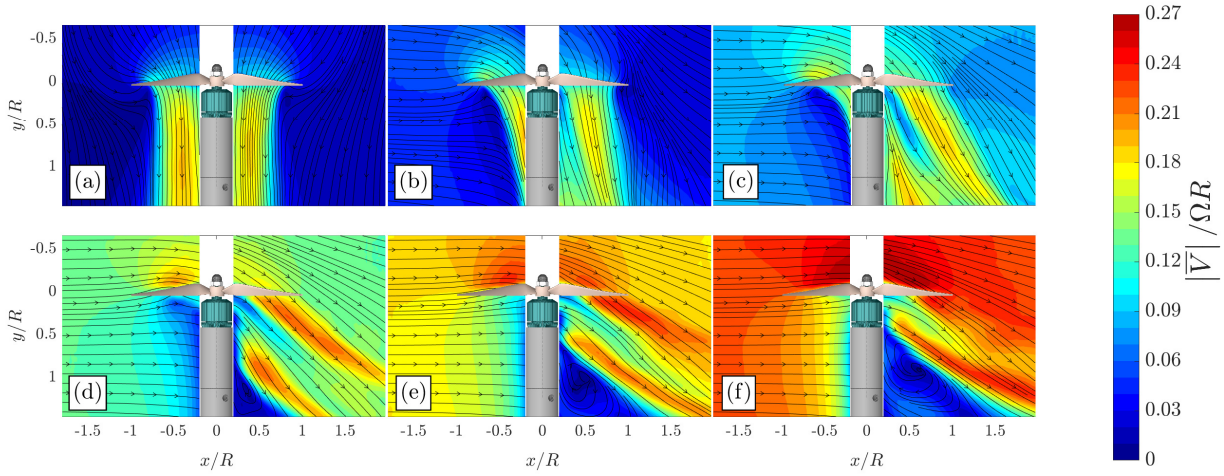

Fig. 9 Colormaps of the normalized time-averaged velocity $|\overline{V}|/\Omega R$ with overlaid streamlines in the x/R-y/R plane. (a) $\mu = 0$, (b) $\mu = 0.04$, (c) $\mu = 0.08$, (d) $\mu = 0.13$, (e) $\mu = 0.17$, (f) $\mu = 0.21$.

In the hovering condition, as shown in figure 9.(a), the wake mainly develops in the axial direction. The propeller operates in still air, inducing a velocity field in the wake region which reaches values up to around 0.19 ΩR. At values of μ greater than 0, the flow field loses its symmetry with respect to the y axis. Already at small values of μ, the flow field topology appears to be significantly affected by the cross-flow, as reported in figures 9.(b) and 9.(c). The wake generated by the blade passing in the fore ROI indeed begins to be visible in the aft ROI. In the cases characterized by greater μ values (figures 9.(d), 9.(e) and 9.(f)), the wake generated in the fore ROI becomes to be mostly visible in the aft region, while the fore ROI is only characterized by the progressive deceleration of the flow impacting against the propeller support. In addition to this, a large recirculating flow region, identifiable by the local streamlines pattern, is generated in the aft ROI. Such low speed structure grows in size at higher μ values, due to a stronger wake deflection.

For what instead concerns the propeller's inlet region, located above the propeller itself, it is clear that the streamlines are deflected towards the x direction due to the presence of the cross-flow. Such deflection becomes more evident as μ increases. In particular, at $\mu = 0.21$ (figure 9.(f)), the streamtube entering the propeller results to be aligned with the x axis in the fore ROI, to then deviate towards the aft ROI, owing to the momentum transfer of the propeller blades. The different streamlines orientation close to the propeller are quantitatively compared by evaluating the orientation angle $\Phi = atan(\overline{V_y}/\overline{V_x})$ of the local velocity vectors at $y/R = 0$. The angle Φ as a function of x/R for the different cases is reported in figure 10, where $\Phi = 0°$ indicates a velocity aligned with the x axis.

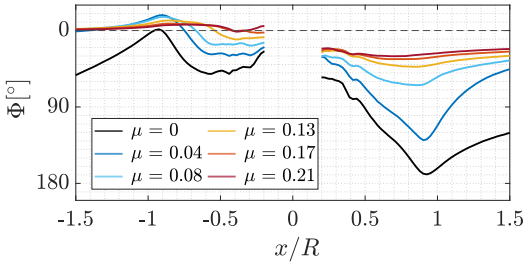

Fig. 10 Velocity vectors orientation angle Φ as a function of x/R evaluated at $y/R = 0$ for the cases shown in figure 9.

The velocity vectors located in the propeller's inlet region tend to orientate in the x direction as μ is increased. Especially in the fore ROI, the Φ profiles obtained for $\mu = 0.17$ and 0.21 are representative of a velocity almost aligned with the x axis. Figure 11 shows the colormaps with overlaid streamlines for the axial velocity component $\overline{V_y}/\Omega R$ at the same μ values.

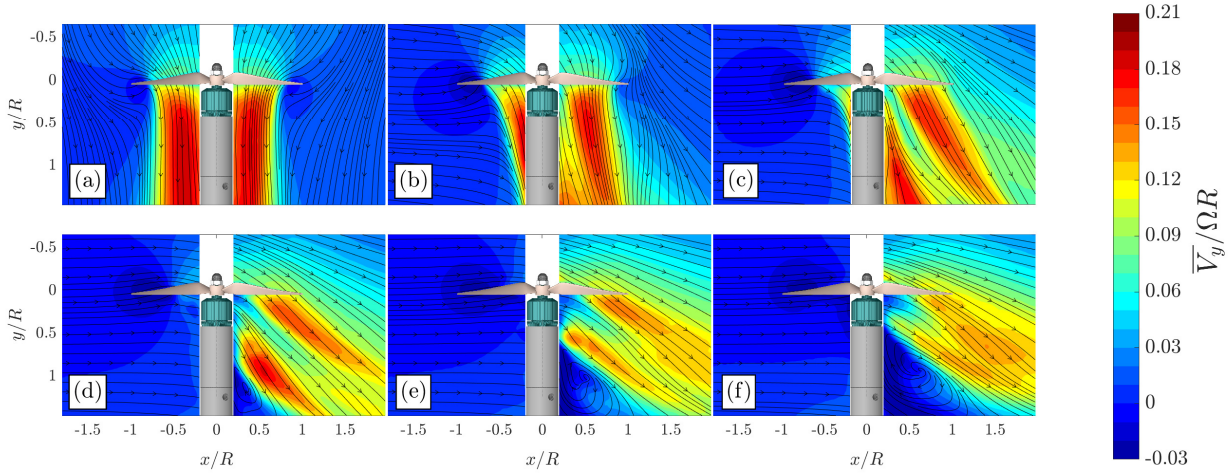

Fig. 11 Colormaps of the normalized time-averaged velocity $\overline{V_y}/\Omega R$ with overlaid streamlines in the x/R-y/R plane. (a) $\mu = 0$, (b) $\mu = 0.04$, (c) $\mu = 0.08$, (d) $\mu = 0.13$, (e) $\mu = 0.17$, (f) $\mu = 0.21$.

The axial velocity $\overline{V_y}/\Omega R$ decreases in the wake region as μ is increased. The wake indeed gains momentum in

the x direction at the expense of the y direction. The $\overline{V_y}/\Omega R$ values extracted at $y/R = 0$ are representative of the non-dimensional induced velocity λ_i distribution at the propeller plane. Such velocity profiles are displayed in figure 12 for a more detailed comparison.

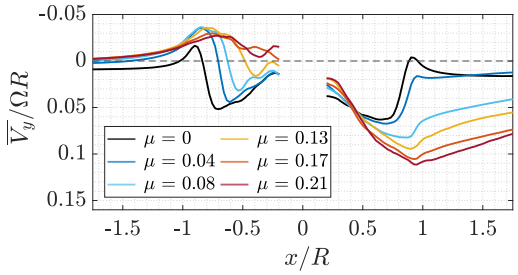

Fig. 12 $\overline{V_y}/\Omega R$ as a function of x/R extrapolated at $y/R = 0$.

In the hovering condition ($\mu = 0$), the velocity profile is approximately symmetric with respect to the propeller's rotation axis, located at $x/R = 0$. Outside of the propeller disk, the velocity assumes a small constant value, while reaches a local minimum at x/R = -1 and $x/R = 1$. These minima are caused by the presence of strong tip vortices, which locally induce a negative velocity on the flow. The flow is advected in the axial direction in the region between x/R > -1 and x/R < 1. As x/R approaches 0, a gradual decrease in $\overline{V_y}/\Omega R$ can be noted. This is mostly due to the lower tangential speed of the blades close to the hub, and to the presence of the propeller's support, which generates a blocking effect on the flow. The presence of the cross-flow alters the symmetry observed between the fore and the aft ROI in the hovering condition. In the fore ROI, $\overline{V_y}/\Omega R$ tends to averagely decrease as μ is increased. Furthermore, both the local minimum and the maximum are shifted towards the cross-flow direction. On the other hand, in the aft ROI it is observed an increase in the $\overline{V_y}/\Omega R$ velocity with a stronger cross-flow.

The analysis of the propeller's wake can be further expanded to account for the distribution of the higher order statistics. The colormaps of the non-dimensional turbulent kinetic energy $\left(k/(\Omega R)^2 = 1/2(\overline{V_x'^2} + \overline{V_y'^2})/(\Omega R)^2\right)$ are plotted in figure 13.

In figures 13.(a) and 13.(b), the largest values of $k/(\Omega R)^2$ are attained in the wake shear layer, where the vortices shed from the blades' tip are located. Furthermore, the wake's portion located in the fore ROI seems to show larger k values as μ increases. For μ greater than 0.08, the wake generated in the fore ROI interacts with the propeller support, resulting in a significant increase in turbulent kinetic energy, which cannot be exclusively associated with the increase in the cross-flow velocity. The wake generated by the cylindrical support plays in fact a role at high cross-flow velocities, considerably affecting the higher order statistics of the flow field generated by the isolated propeller. In figure 13.(b), a small circular region of high k is located under the blade at x/R = -0.75. This can be associated to the average position of the early age strong tip vortices. This local peak of k tends to shift towards greater x/R coordinates as μ increases, until it is not visible anymore in figure 13.(e) and 13.(f). In these cases, the wake generated in the fore ROI results to be

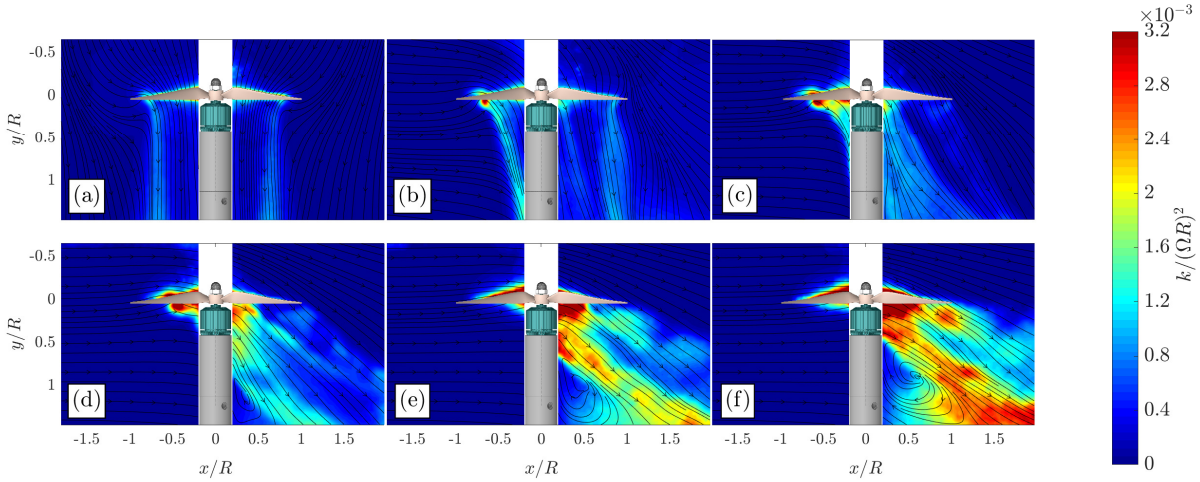

Fig. 13 Colormaps of the normalized time-averaged $k/(\Omega R)^2$ with overlaid streamlines in the x/R-y/R plane. (a) $\mu = 0$, (b) $\mu = 0.04$, (c) $\mu = 0.08$, (d) $\mu = 0.13$, (e) $\mu = 0.17$, (f) $\mu = 0.21$.

almost completely deflected in the aft region. Thus the early age tip vortices end up to interact with the propeller's hub, resulting in an expanded region of high k, which eventually extends also for positive x/R coordinates. The wake's portion generated in the aft ROI exhibits instead a less straightforward behaviour. While the turbulent kinetic energy in the shear layer initially seems to be slightly enhanced from $\mu = 0$ to $\mu = 0.13$, it then undergoes a noticeable drop in the shear layer for the cases in figures 13.(c) and 13.(d). When μ is further increased, a growth in the shear layer's k values is again observable, most likely due to the interaction with the propeller support's wake.

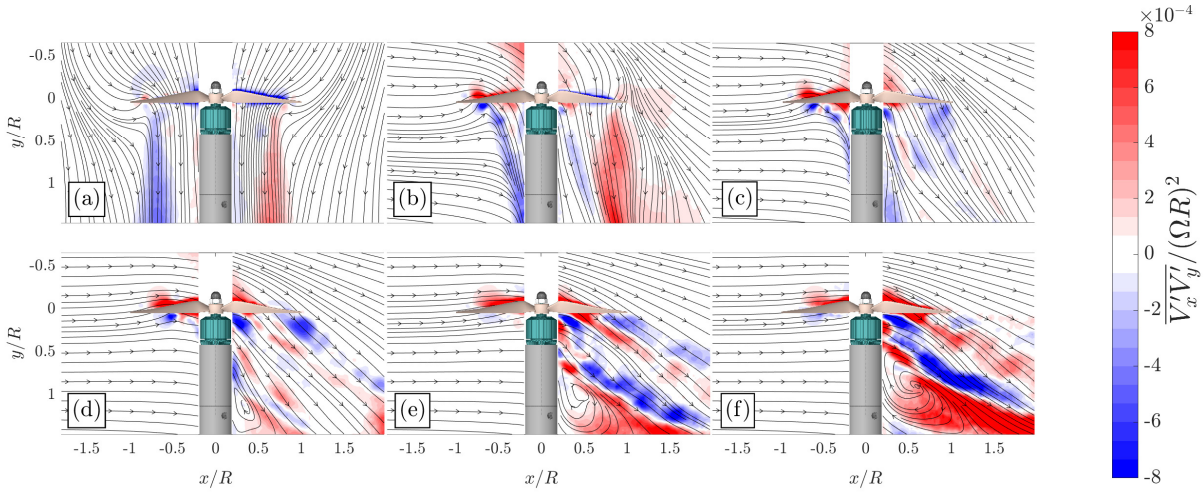

Fig. 14 Colormaps of the normalized time-averaged $\overline{V'_x V'_y}/(\Omega R)^2$ with overlaid streamlines in the x/R-y/R plane. (a) $\mu = 0$, (b) $\mu = 0.04$, (c) $\mu = 0.08$, (d) $\mu = 0.13$, (e) $\mu = 0.17$, (f) $\mu = 0.21$.

Similar considerations can be inferred from the component of the Reynolds stress tensor $\overline{V'_x V'_y}/(\Omega R)^2$, as reported in figure 14. This quantity indicates the evidence of high turbulence dynamics in the flow, which is predominantly

registered in the wake shear layer and close to the propeller's blades. Large negative $\overline{V_x' V_y'}/(\Omega R)^2$ values are in fact obtained in the wake's shear layer generated in the fore ROI. For μ between 0.13 and 0.40, a peak of negative Reynolds stress is registered close to the blade, as reported in figures 14.(b), 14.(c) and 14.(d). As already discussed for the k fields, this local peak represents the average location of the early age tip vortices and it is advected towards the cross-flow direction as μ attains to greater values. As μ is equal to 0.17, this local peak is not anymore present, most likely due to the interaction of the tip vortices with the propeller support. Such interaction additionally contributes to the generation of two distinct high $\overline{V_x' V_y'}/(\Omega R)^2$ zones of opposite signs in the wake shear layer. This is observable mostly in figures 14.(e) and 14.(f), where the support's wake effect starts to be become prominent. The wake generated in the aft ROI undergoes instead a different modification due to the cross-flow presence. In the hovering condition in figure 14.(a), the Reynolds stress distribution appears to be symmetric with respect to the wake in the fore ROI. As μ is increased over 0.13, the positive $\overline{V_x' V_y'}/(\Omega R)^2$ region generated in the wake shear layer is not visible anymore and a region of negative Reynolds stress takes its place. The interaction with the propeller's support generates an additional region of positive $\overline{V_x' V_y'}/(\Omega R)^2$ values, visible for $\mu > 0.17$ which becomes predominant as μ is further increased.

C. Vortical system characterization

The chosen vortices identification method introduced in section II.C is highly prone to vortices misidentification due to its reliance upon empirical thresholding. As a consequence, the choice of a different threshold value Γ_{2-thr} can severely impact the number of identified structures and should be adapted for the specific purpose. In the present work, Γ_{2-thr} was imposed equal to 0.9 after a dedicated investigation carried out on the hovering case. This case presents in fact multiple vortical structures of different dimensions and circulation which are not advected away from the propeller proximity due to the lack of an external flow. In order to properly isolate the vortices of interest, shed by the propeller's tips, it is necessary to choose a significantly high Γ_{2-thr}, which permits to isolate mostly the strongest structures. On the other hand, it is likely that excessively increasing the threshold towards the value of 1 may lead to to the identification of a limited number of vortices, affecting the statistical significance of the results.

To this purpose, the vortex identification was carried out for the hovering case with three different Γ_{2-thr} values and the obtained results are reported in the scatter plots in figure 15. In figure 15.(a), the results of the identification carried out with $\Gamma_{2-thr} = 0.85$ are displayed. With such value, many vortical structures are identified mostly in the wake shear layer, generating a dense region of points where it is not straightforward to isolate the strongest structures. By increasing Γ_{2-thr} to 0.9, as reported in figure 15.(b), the strongest structures become more visible as the weakest vortices are neglected. If the threshold value Γ_{2-thr} is further increased to 0.95, the tip vortices are not identified and consequently not represented in the scatter plot in figure 15.(c). As a result of this analysis, the authors opted for $\Gamma_{2-thr} = 0.9$ for the current investigation.

The vortical structures identified with the use of the Γ_2 criterion, mentioned in section II.C, are reported in the

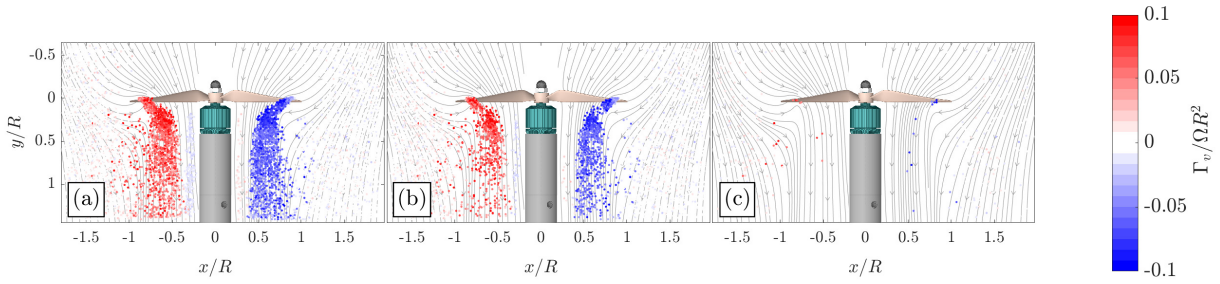

Fig. 15 Scatter plots of the identified vortical structures in the hovering condition (μ = 0) at different threshold values Γ_{2-thr}. (a) Γ_{2-thr} = 0.85, (b) Γ_{2-thr} = 0.9, (c) Γ_{2-thr} = 0.95.

scatter plots in figure 16. In particular, the vortices are displayed in correspondence of their identified centers as fixed size dots, with a color scale that characterizes their dimensionless circulation. The circulation Γ_v is calculated with the use of Stokes-Kelvin theorem, as the integral of the vorticity field in the area of a given vortex. As previously mentioned in section II.C, the vortex area corresponds to a singularly connected region whose points present $|\Gamma_2| > 2/\pi$, calculated with the use of eq. 9. For the current analysis, a Γ_{2-thr} value of 0.9 was finally taken into account at each value of μ.

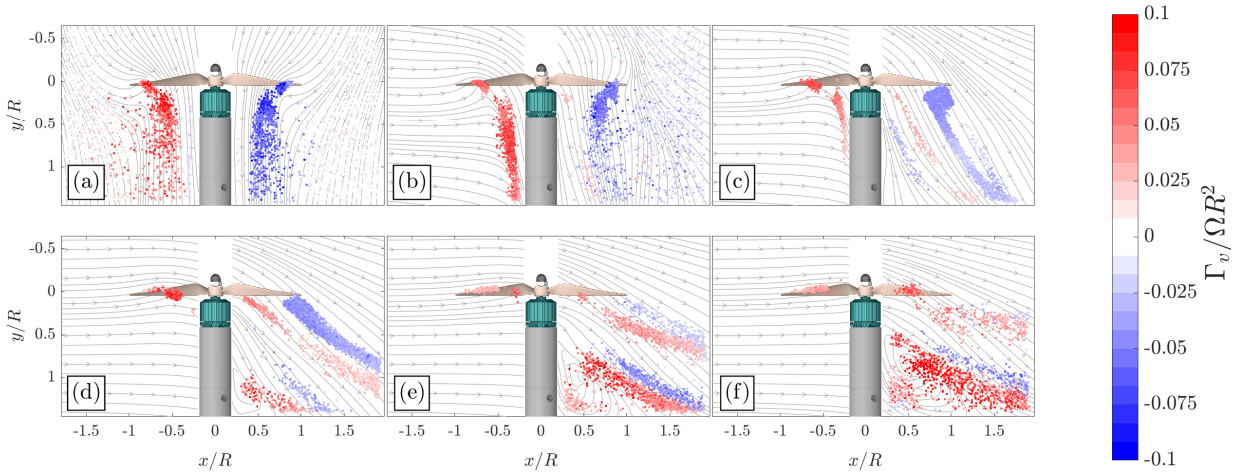

Fig. 16 Scatter plots of the identified vortical structures with overlaid streamlines in the x/R-y/R plane. (a) μ = 0, (b) μ = 0.04, (c) μ = 0.08, (d) μ = 0.13, (e) μ = 0.17, (f) μ = 0.21.

In figure 16.(a), two main aggregations of vortical structures are respectively visible in the fore and aft ROI. Such structures are shed from the blades' tip and show a strong circulation of opposite sign in the two regions. Their circulation additionally tends to decrease in absolute value with the distance from the blades. Once they are shed from the blades, the tip vortices tend to move closer to the propeller's hub, as a cumulative effect of the wake shrinking caused by the local acceleration and their own induced velocity. Their mean trajectory is however not well defined along a clear path and presents a significant scattering in the direction of the cross-flow. In the absence of an external

inflow, the vortices are advected away from the propeller exclusively by the induced velocity generated in the wake. The propeller in hover conditions hence works in less uniform air conditions, which might result into a drop in the propulsive efficiency [54]. The tip vortices end up scattering outside of the wake and are still visible in the flow field despite of their significantly damped circulation. Further weak vortices can be detected close to the rotor hub. These structures represent the vortices shed from the propeller's root, respectively in the fore and aft ROI, and their circulation might be enhanced by the interaction with the propeller's support.

As μ is increased, even small cross-flow velocities lead to major changes in the vortices distribution. In the fore ROI, the tip vortices present a clearer pattern with respect to the hovering condition. At μ = 0.04 and 0.08 (figures 16.(b) and 16.(c)), the tip vortices appear to be confined to a well-defined trajectory and are shifted towards greater x/R coordinates as μ is increased. As the advance ratio is increased above 0.08, the early age tip vortices undergo a strong deflection along the blade-span, eventually interacting with the following passing blades. Such early age vortices averagely are characterized by a small circulation value, thus if the blades-vortex interaction results on one hand more frequent with a stronger cross-flow velocity, the vortices involved in this interaction present a damped circulation, consequently containing the downsides of this phenomenon. The tip vortices are then advected downstream and become visible in the aft ROI for $\mu > 0.13$. In figures 16.(d), 16.(e) and 16.(f), the streamlines orientation close to the propeller's support indicates the presence of a major flow recirculation, already discussed in terms of time-averaged flow features when presenting figure 11. In this region, the propeller's wake vortices interact with the propeller support's wake, generating a vortical macro-structure and locally enhancing the tip vortices circulation. The root vortices are also advected in the aft ROI and are displayed with a greater circulation as μ is increased.

For what regards instead the vortices generated in the aft ROI, it is necessary to make different considerations. The blue-colored tip vortices are damped in circulation and organized in more defined trajectories as μ is increased. As μ is increased above 0.17, their circulation is reduced to the extent that they are not almost visible anymore in the region of interest. At μ = 0.21 as reported in figure 16.(f), only a few vortical structures with negative value of Γ_v are detected close to the blades' tip, indication that the downstream tip vortices are disrupted by the interaction with the cross-flow and possibly swept away from the blade owing to the cross-stream velocity. In the same region, some weak vortices with a positive circulation become predominant as μ is increased. Such vortices are generated by the blades' root and display an opposite behaviour with respect to the tip vortices. Their circulation is increased as μ is increased, due to the interaction with the support's wake. Furthermore, at μ = 0.21, multiple vortices with positive circulation are detected on the blades. As previously observed in the fore ROI, the presence of the cross-flow contributes to the enhancement of the blades-vortex interaction, by displacing the early age vortical structures along the blade-span direction and not in the axial direction as an axial inflow would do.

In the aft ROI for $\mu > 0.13$, it is possible to notice a misalignment between the tip vortices trajectory and the flow fields' streamlines. This effect might be due to an intrinsic flaw of the chosen methodology for the vortices identification,

since it properly works when the vorticity is mostly aligned with the out-of-plane direction. In the hovering case, the vorticity is indeed expected to be mostly directed towards the out-of-plane direction in the wake shear layer and the remaining vorticity components can be neglected. While this is true in the hovering case, it is not straightforward to predict how the vorticity components evolve with the increase of the cross-flow velocity. For instance in [55], the authors observed the formation of a large horseshoe vortex oriented in the cross-flow direction since very contained μ values. A considerable increase of the vorticity components along x and y might in fact lead to a misidentification of the tip vortices centers and a miscalculation of their circulation since they might not be mostly aligned with the out-of-plane axis. While this aspect is surely of interest, it is not within the capabilities of the current measurement approach. Indeed, it would be necessary to retrieve all the vorticity components with the use of different PIV setups, among which the tomographic PIV, or through CFD simulations of the rotating propeller.

IV. Conclusions

In the present study, an experimental campaign was carried out on a small drone propeller in forward flight conditions. The propeller is characterized by a small value of the chord-based Reynolds number, which leads to numerous challenges in the numerical predictions of its performance and induced flow field. The propeller was characterized in thrust and torque at different values of the advance ratio μ. The experimental data were interpolated with the use of semi-empirical equations derived from the field of helicopters' design. The interpolation led to a satisfactory fitting and the computed corrective coefficients resulted to be very close to the ones used in literature. The small differences are most likely attributable to the small Reynolds numbers and the high pitch which characterize the investigated drone propeller and are not peculiar of larger helicopters' rotors. The propeller's mean blade profile drag coefficient was evaluated from its drag coefficient at zero angle of attack with the use of a third corrective coefficient. The value of this coefficient might be generalizable for different geometries and operative conditions, but there would be the need of further experimental campaigns focused on the topic.

Flow field measurements were carried out with the use of the planar PIV. The main findings showed a significant deflection of the velocity vectors in the propeller's inlet and wake regions towards the direction of the cross-flow, even for contained advance ratios. The flow field's higher order statistics as the turbulent kinetic energy and the cross-component of the Reynolds stress tensor were inspected. Both quantities showed local increases in the wake shear layer as the advance ratio was increased. The major effects were however due to the interaction with rotor support, which led to a significant local enhancement of both quantities.

In conclusion, a thorough analysis of the vortical structures evolution in the different cases was carried out with the use of the Γ_2 criterion. The strongest vortices were found to be located in the propeller's wake shear layer, after having been shed by the blades' tip. With respect to the hovering case, the vortices resulted to be confined in more defined trajectories due to the presence of an external cross-flow. The tip and root vortices generated by the upstream passing

blades resulted to be enhanced in circulation with the increase of the cross-flow velocity. On the other hand, the tip vortices generated downstream appeared to be damped by the cross-flow, while the root vortices still resulted to be enhanced, due also to the the interaction with the propeller's support.

The experimental campaign carried out in this work aimed to analyze in details the aerodynamics of a small-scale propeller in forward flight. Further flow and performance features can be inferred with the use of low and high fidelity computational methods, if adequately adapted for the low Reynolds numbers regimes. CFD URANS simulations and mid-fidelity VPM simulations are currently ongoing with the aim of replicating the experimental results and give additional insights on the occurring phenomena. In addition, different propellers' geometries and angles of attack with respect to the inflow need to be investigated to further extend and validate the proposed modifications of the semi-empirical formulas from the literature to small-scaled propellers. The open and easily replicable geometry of the present propeller is intended to ensure a continuity of research in this area, with the goal of expanding the scientific community's knowledge of such complex operative conditions.

Funding Sources

This work is part of the project PNRR-NGEU which has received funding from the MUR-DM352/2022. This study was carried out within the MOST – Sustainable Mobility National Research Center and received funding from the European Union Next-GenerationEU (PIANO NAZIONALE DI RIPRESA E RESILIENZA (PNRR) – MISSIONE 4 COMPONENTE 2, INVESTIMENTO 1.4 – D.D. 1033 17/06/2022, CN00000023). This manuscript reflects only the authors' views and opinions, neither the European Union nor the European Commission can be considered responsible for them.

Acknowledgments

G. A. acknowledges ONERA for co-sponsoring the PhD studentship. The authors acknowledge the members of the team EoliTo for the use of the 3D printer and the research assistant Manuel Carreno Ruiz for his precious help in the analysis of some of the results.

References

[1] Hussain, A., and D., S., "Advanced air mobility - Can the United States afford to lose the race?" Tech. rep., Deloitte Consulting, 2021. URL https://www2.deloitte.com/us/en/insights/industry/aerospace-defense/advanced-air-mobility.html.

[2] Puri, V., Nayyar, A., and Raja, L., "Agriculture drones: A modern breakthrough in precision agriculture," *Journal of Statistics and Management Systems*, Vol. 20, No. 4, 2017, pp. 507–518. https://doi.org/https://doi.org/10.1080/09720510.2017.1395171.

[3] Cheng, E., *Aerial photography and videography using drones*, Peachpit Press, 2015.

[4] Sauls, L. A., Paneque-Gálvez, J., Amador-Jiménez, M., Vargas-Ramírez, N., and Laumonier, Y., "Drones, communities and nature: pitfalls and possibilities for conservation and territorial rights," *Global Social Challenges Journal*, Vol. 2, No. 1, 2023, pp. 24–46. https://doi.org/https://doi.org/10.1332/AJHA9183.

[5] Mueller, T. J., and DeLaurier, J. D., "Aerodynamics of small vehicles," *Annual review of fluid mechanics*, Vol. 35, No. 1, 2003. https://doi.org/https://doi.org/10.1146/annurev.fluid.35.101101.161102.

[6] Milluzzo, J., and Leishman, J. G., "Fluid dynamics of the helicoidal wake sheets trailed from a hovering rotor," *Journal of the American Helicopter Society*, Vol. 61, No. 1, 2016, pp. 1–17. https://doi.org/https://doi.org/10.4050/JAHS.61.012002.

[7] Ning, Z., and Hu, H., "An experimental study on the aerodynamic and aeroacoustic performances of a bio-inspired UAV propeller," *35th AIAA Applied Aerodynamics Conference*, 2017, p. 3747. https://doi.org/https://doi.org/10.2514/6.2017-3747.

[8] Podsędkowski, M., Konopiński, R., Obidowski, D., and Koter, K., "Variable pitch propeller for UAV-experimental tests," *Energies*, Vol. 13, No. 20, 2020, p. 5264. https://doi.org/https://doi.org/10.3390/en13205264.

[9] Ruiz, M. C., Scanavino, M., D'Ambrosio, D., Guglieri, G., and Vilardi, A., "Experimental and numerical analysis of hovering multicopter performance in low-Reynolds number conditions," *Aerospace Science and Technology*, Vol. 128, 2022, p. 107777. https://doi.org/https://doi.org/10.1016/j.ast.2022.107777.

[10] Pérez Gordillo, A. M., Villegas Santos, J. S., Lopez Mejia, O. D., Suarez Collazos, L. J., and Escobar, J. A., "Numerical and experimental estimation of the efficiency of a quadcopter rotor operating at hover," *Energies*, Vol. 12, No. 2, 2019, p. 261. https://doi.org/https://doi.org/10.3390/en12020261.

[11] Pérez Gordillo, A. M., Escobar, J. A., and Lopez Mejia, O. D., "Influence of the Reynolds Number on the Aerodynamic Performance of a Small Rotor," *Aerospace*, Vol. 10, No. 2, 2023, p. 130. https://doi.org/https://doi.org/10.3390/aerospace10020130.

[12] Grande, E., Romani, G., Ragni, D., Avallone, F., and Casalino, D., "Aeroacoustic investigation of a propeller operating at low reynolds numbers," *AIAA Journal*, Vol. 60, No. 2, 2022, pp. 860–871. https://doi.org/https://doi.org/10.2514/1.J060611.

[13] Grande, E., Ragni, D., Avallone, F., and Casalino, D., "Laminar separation bubble noise on a propeller operating at low Reynolds numbers," *AIAA Journal*, Vol. 60, No. 9, 2022, pp. 5324–5335. https://doi.org/https://doi.org/10.2514/1.J061691.

[14] Grava, A., Picillo, M., Serpieri, J., Iuso, G., Bernardos, L., and Cafiero, G., "Aerodynamic investigation of a drone propeller in cross-flow," *AIAA SCITECH 2024 Forum*, 2024, p. 0244. https://doi.org/https://doi.org/10.2514/6.2024-0244.

[15] Yang, Y., Liu, Y., Li, Y., Arcondoulis, E., and Wang, Y., "Aerodynamic and aeroacoustic performance of an isolated multicopter rotor during forward flight," *AIAA Journal*, Vol. 58, No. 3, 2020, pp. 1171–1181. https://doi.org/https://doi.org/10.2514/1.J058459.

[16] Cerny, M., and Breitsamter, C., "Investigation of small-scale propellers under non-axial inflow conditions," *Aerospace Science and Technology*, Vol. 106, 2020, p. 106048. https://doi.org/https://doi.org/10.1016/j.ast.2020.106048.

[17] Jamaluddin, N. S., Celik, A., Baskaran, K., Rezgui, D., and Azarpeyvand, M., "Aerodynamic noise analysis of tilting rotor in edgewise flow conditions," *Journal of Sound and Vibration*, Vol. 582, 2024, p. 118423. https://doi.org/https://doi.org/10.1016/j.jsv.2024.118423.

[18] Kolaei, A., Barcelos, D., and Bramesfeld, G., "Experimental Analysis of a Small-Scale Rotor at Various Inflow Angles," *International Journal of Aerospace Engineering*, Vol. 2018, No. 1, 2018, p. 2560370. https://doi.org/https://doi.org/10.1155/2018/2560370.

[19] Cai, J., and Gunasekaran, S., "Frequency Response of RC Propellers to Streamwise Gusts in Forward Flight," *Wind*, Vol. 3, No. 2, 2023, pp. 253–272. https://doi.org/https://doi.org/10.3390/wind3020015.

[20] Goldschmidt, J., Tingle, H., Ifju, P., Miller, S., Ukeiley, L., Goldman, B., Droandi, G., and Lee, K., "Acoustics and Forces from a Subscale Electric Vertical-Takeoff-and-Landing Rotor in Edgewise Flight," *AIAA Journal*, 2024, pp. 1–16. https://doi.org/https://doi.org/10.2514/1.J063568.

[21] Newman, S., "Principles of Helicopter Aerodynamics–Second edition JG Leishmann Cambridge University Press, The Edinburgh Building, Shaftesbury Road, Cambridge, CB2 2RU, UK. 2006. 826pp. Illustrated.£ 65. ISBN 0-521-85860-7." *The Aeronautical Journal*, Vol. 111, No. 1126, 2007, pp. 825–826.

[22] Brotherhood, P., and Stewart, W., "An experimental investigation of the flow through a helicopter rotor in forward flight," 1949.

[23] Cheeseman, I., and Bennett, W., "The effect of the ground on a helicopter rotor in forward flight," 1955.

[24] Rajagopalan, R. G., and Mathur, S. R., "Three dimensional analysis of a rotor in forward flight," *Journal of the American Helicopter Society*, Vol. 38, No. 3, 1993, pp. 14–25. https://doi.org/https://doi.org/10.4050/JAHS.38.14.

[25] Berenger, T., Favier, D., Maresca, C., and Berton, E., "Experimental and numerical investigation of rotor aerodynamics in forward flight," *Journal of aircraft*, Vol. 34, No. 3, 1997, pp. 394–399. https://doi.org/https://doi.org/10.2514/2.2182.

[26] Steijl, R., Barakos, G., and Badcock, K., "A framework for CFD analysis of helicopter rotors in hover and forward flight," *International journal for numerical methods in fluids*, Vol. 51, No. 8, 2006, pp. 819–847. https://doi.org/https://doi.org/10.1002/fld.1086.

[27] Yaakub, M., Wahab, A., Abdullah, A., Mohd, N. N., and Shamsuddin, S., "Aerodynamic prediction of helicopter rotor in forward flight using blade element theory," *Journal of Mechanical Engineering and Sciences*, Vol. 11, No. 2, 2017, pp. 2711–2722. https://doi.org/https://doi.org/10.15282/jmes.11.2.2017.12.0246.

[28] Badrya, C., Govindarajan, B., and Chopra, I., "Basic understanding of unsteady airfoil aerodynamics at low Reynolds numbers," *2018 AIAA Aerospace Sciences Meeting*, 2018, p. 2061. https://doi.org/https://doi.org/10.2514/6.2018-2061.

[29] Casalino, D., Grande, E., Romani, G., Ragni, D., and Avallone, F., "Definition of a benchmark for low Reynolds number propeller aeroacoustics," *Aerospace Science and Technology*, Vol. 113, 2021, p. 106707. https://doi.org/https://doi.org/10.1016/j.ast.2021.106707.

[30] Jardin, T., Prothin, S., and Magaña, C., "Aerodynamic performance of a hovering microrotor in confined environment," *Journal of the American Helicopter Society*, Vol. 62, No. 2, 2017, pp. 1–7. https://doi.org/https://doi.org/10.4050/JAHS.62.022008.

[31] Prothin, S., Fernandez Escudero, C., Doué, N., and Jardin, T., "Aerodynamics of MAV rotors in ground and corner effect," *International Journal of Micro Air Vehicles*, Vol. 11, 2019, p. 1756829319861596. https://doi.org/https://doi.org/10.1177/1756829319861596.

[32] Nardari, C., Casalino, D., Polidoro, F., Coralic, V., Lew, P., and Brodie, J., "Numerical and experimental investigation of flow confinement effects on UAV rotor noise," *25th AIAA/CEAS Aeroacoustics Conference*, 2019, p. 2497. https://doi.org/https://doi.org/10.2514/6.2019-2497.

[33] Lee, T. E., Leishman, J. G., and Ramasamy, M., "Fluid dynamics of interacting blade tip vortices with a ground plane," *Journal of the American Helicopter Society*, Vol. 55, No. 2, 2010, pp. 22005–22005. https://doi.org/https://doi.org/10.4050/JAHS.55.022005.

[34] Astarita, T., and Cardone, G., "Analysis of interpolation schemes for image deformation methods in PIV," *Experiments in fluids*, Vol. 38, 2005, pp. 233–243. https://doi.org/https://doi.org/10.1007/s00348-004-0902-3.

[35] Astarita, T., "Analysis of velocity interpolation schemes for image deformation methods in PIV," *Experiments in Fluids*, Vol. 45, 2008, pp. 257–266. https://doi.org/https://doi.org/10.1007/s00348-008-0475-7.

[36] Astarita, T., "Analysis of weighting windows for image deformation methods in PIV," *Experiments in fluids*, Vol. 43, 2007, pp. 859–872. https://doi.org/https://doi.org/10.1007/s00348-007-0314-2.

[37] Sciacchitano, A., and Wieneke, B., "PIV uncertainty propagation," *Measurement Science and Technology*, Vol. 27, No. 8, 2016, p. 084006. https://doi.org/https://doi.org.10.1088/0957-0233/27/8/084006.

[38] Glauert, H., and Ministry, G. B. A., *On the horizontal flight of a helicopter*, Reports and Memoranda ; No. 1157, H.M. Stationery Office, 1928. URL https://books.google.fr/books?id=hVPrMgEACAAJ.

[39] Kim, K. C., "Analytical calculations of helicopter torque coefficient (CQ) and thrust coefficient (CT) values for the Helicopter Performance (HELPE) model," *US Army Research Laboratory*, 1999.

[40] Johnson, W., *Helicopter theory*, Courier Corporation, 2012.

[41] Winslow, J., Otsuka, H., Govindarajan, B., and Chopra, I., "Basic understanding of airfoil characteristics at low Reynolds numbers (10 4–10 5)," *Journal of aircraft*, Vol. 55, No. 3, 2018, pp. 1050–1061. https://doi.org/https://doi.org/10.2514/1.C034415.

[42] Wang, S., Zhou, Y., Alam, M. M., and Yang, H., "Turbulent intensity and Reynolds number effects on an airfoil at low Reynolds numbers," *Physics of Fluids*, Vol. 26, No. 11, 2014. https://doi.org/https://doi.org/10.1063/1.4901969.

[43] Drela, M., "XFOIL: An analysis and design system for low Reynolds number airfoils," *Low Reynolds Number Aerodynamics: Proceedings of the Conference Notre Dame, Indiana, USA, 5–7 June 1989*, Springer, 1989, pp. 1–12. https://doi.org/https://doi.org/10.1007/978-3-642-84010-4_1.

[44] Van Ingen, J., "The eN method for transition prediction. Historical review of work at TU Delft," *38th Fluid Dynamics Conference and Exhibit*, 2008, p. 3830. https://doi.org/https://doi.org/10.2514/6.2008-3830.

[45] Jeong, J., and Hussain, F., "On the identification of a vortex," *Journal of Fluid Mechanics*, Vol. 285, 1995, p. 69–94. https://doi.org/https://doi.org/10.1017/S0022112095000462.

[46] Hunt, J., Wray, A., and Moin, P., "Eddies, streams, and convergence zones in turbulent flows," *Studying Turbulence Using Numerical Simulation Databases*, Vol. -1, 1988, pp. 193–208.

[47] Dallmann, U., "Topological structures of three-dimensional vortex flow separation," *16th Fluid and Plasmadynamics Conference*, 1983. https://doi.org/https://doi.org/10.2514/6.1983-1735.

[48] De Gregorio, F., and Visingardi, A., "Vortex detection criteria assessment for PIV data in rotorcraft applications," *Experiments in Fluids*, Vol. 61, 2020, pp. 1–22. https://doi.org/https://doi.org/10.1007/s00348-020-03012-7.

[49] Graftieaux, L., Michard, M., and Grosjean, N., "Combining PIV, POD and vortex identification algorithms for the study of unsteady turbulent swirling flows," *Measurement Science and technology*, Vol. 12, No. 9, 2001, p. 1422. https://doi.org/https://doi.org/10.1088/0957-0233/12/9/307.

[50] Cafiero, G., Castrillo, G., Greco, C., and Astarita, T., "On the effects of square-fractal turbulators on the flow field generated by a synthetic jet actuator," *Experimental Thermal and Fluid Science*, Vol. 102, 2019, pp. 302–315. https://doi.org/https://doi.org/10.1016/j.expthermflusci.2018.12.005.

[51] De Gregorio, F., Visingardi, A., and Iuso, G., "An experimental-numerical investigation of the wake structure of a hovering rotor by piv combined with a Γ_2 vortex detection criterion," *Energies*, Vol. 14, No. 9, 2021, p. 2613. https://doi.org/https://doi.org/10.3390/en14092613.

[52] Soto-Valle, R., Cioni, S., Bartholomay, S., Manolesos, M., Nayeri, C., Bianchini, A., and Paschereit, C. O., "Vortex identification methods applied to wind turbine tip vortices," *Wind Energy Science*, Vol. 7, No. 2, 2022, pp. 585–602. https://doi.org/https://doi.org/10.5194/wes-7-585-2022.

[53] Slinker, B. K., and Glantz, S. A., *Primer of applied regression and analysis of variance*, McGraw-Hill, 1990.

[54] FAA, *Helicopter Flying Handbook*, United States Department of Transportation, Federal Aviation Administration, Airman Testing Branch, P.O. Box 25082, Oklahoma City, OK 73125, 2019.

[55] Bloise, N., Ruiz, M. C., D'Ambrosio, D., and Guglieri, G., "Preliminary design of a remotely piloted aircraft system for crop-spraying on vineyards," *2020 IEEE International Workshop on Metrology for Agriculture and Forestry (MetroAgriFor)*, IEEE, 2020, pp. 1–6. https://doi.org/https://doi.org/10.1109/MetroAgriFor50201.2020.927760.